Earth and Planetary Science Letters 412 (2015) 101–111

Contents lists available at ScienceDirect

Earth and Planetary Science Letters

www.elsevier.com/locate/epsl

Receiver function images of the mantle transition zone beneath NE China: New constraints on intraplate volcanism, deep subduction and their potential link

Zheng Liu [a,b], Fenglin Niu [c,b,*], Yongshun John Chen [a], Steve Grand [d], Hitoshi Kawakatsu [e], Jieyuan Ning [a], Satoru Tanaka [f], Masayuki Obayashi [f], James Ni [g]

[a] Institute of Theoretical and Applied Geophysics, Peking University, Beijing, China
[b] Department of Earth Science, Rice University, Houston, USA
[c] State Key Laboratory of Petroleum Resource and Prospecting, and Unconventional Natural Gas Institute, China University of Petroleum, Beijing, China
[d] Department of Geological Sciences, University of Texas at Austin, Austin, USA
[e] Earthquake Research Institute, University of Tokyo, Tokyo, Japan
[f] Institute for Frontier Research on Earth and Evolution, Japan Agency for Marine–Earth Science and Technology, Yokosuka, Japan
[g] Department of Physics, New Mexico State University, Las Cruces, USA

ARTICLE INFO

Article history:
Received 30 April 2014
Received in revised form 4 December 2014
Accepted 7 December 2014
Available online 6 January 2015
Editor: P. Shearer

Keywords:
mantle discontinuities
phase transition
receiver function
NE China
deep subduction
intraplate volcanism

ABSTRACT

In order to better understand the deep subduction geometry of the Pacific plate and genesis of intraplate volcanism in northeast China (NE China), we computed a total of 45,505 receiver functions from 788 teleseismic events recorded by 255 stations (NECESSArray temporal and permanent stations) in NE China. We used a common-conversion-point stacking (CCP) method to generate a 3D reflectivity volume beneath the study area. To position the P-to-S conversions to the correct depths, we employed 3D crustal and mantle models as references to make time to depth conversion. The 3D reflectivity volume was generated in an area between 115°–135°E and 40°–49°N, in the depth range of 300 to 800 km. We found significant topographic relief on the 660-km discontinuity across the study area. In particular, in a westward Pacific plate subduction section between 40°N and ~45.5°N, the 660-km discontinuity is depressed by as much as ~30–40 km along the western extension of the deep seismicity. The depression is elongated along the strike of the deep seismicity and is confined to a 200–300 km region in the E–W direction of subduction. To the west of this depression the 660-km discontinuity is uplifted by 5–10 km in a rectangular area of ~100 km by 200 km centered at about 125°E and 43°N. In the north, the 660-km discontinuity is moderately depressed (~20 km) in a broad area that extends further west. The high and low regions in the 660-km topographic map correlate, respectively, with low- and high-velocity anomalies in the P- and S-wave tomographic velocity images at the same depth. Our results suggest that slab stagnation might not be occurring in the southern part of the NE China, where the Changbaishan volcanic complex is located, thus the magmatism is unlikely caused by dehydration of the flat-lying Pacific slab in the transition zone. The low velocity mantle upwelling arising from a gap of stagnant slabs is a likely source that feeds the volcanic complex in NE China.

1. Introduction

Northeast China (NE China) consists of the northeast China plain (Songliao Basin) in its center, the Great Xing'an Range in the west, and the Changbai Mountain Range (as known as Paektu in North Korea, Baekdu in South Korea) in the southeast. NE China is presently located ~1300 km away from the Japan Trench where the Pacific plate begins subducting and reaches approximately 600 km deep near the eastern edge of the area (Fig. 1). Many tomography models (Fukao et al., 2003; Huang and Zhao, 2006; Li and van der Hilst, 2010; Wei et al., 2012) suggest that the subducting Pacific plate starts to bend upward and lies flat within the transition zone beneath NE China. The total length of the high velocity anomaly revealed by these models is <2000 km, much less than the estimate based on plate reconstruction (Engebretson et al., 1992), which shows that roughly 5000 km of Pacific plate has subducted at the Japan Trench during the past 50 Ma. The

* Corresponding author at: State Key Laboratory of Petroleum Resource and Prospecting, and Unconventional Natural Gas Institute, China University of Petroleum at Beijing, Beijing, China. Tel.: +86 10 8973 9080.
E-mail address: niu@cup.edu.cn (F. Niu).

http://dx.doi.org/10.1016/j.epsl.2014.12.019
0012-821X/

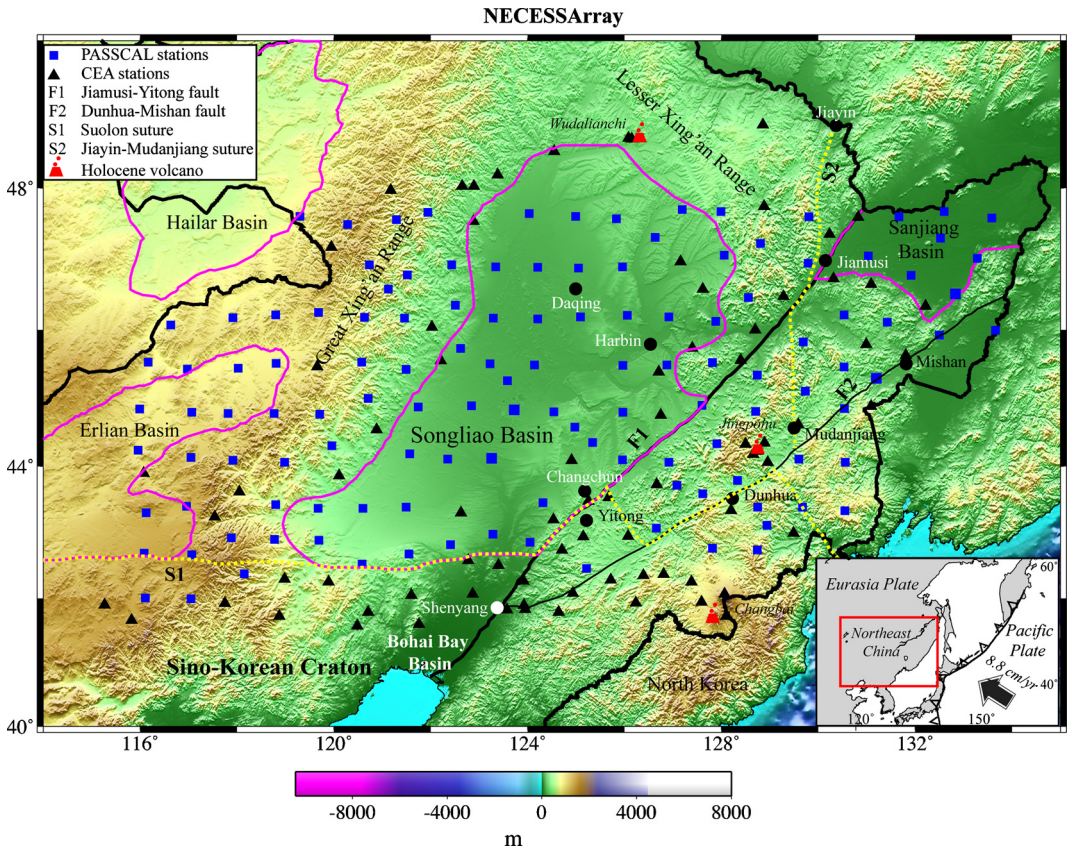

Fig. 1. Map showing topography, major faults, and tectonic units of NE China. The purple lines outline major basins in the area. The black solid lines and the dotted yellow lines represent the large strike-slip faults and major suture zones, respectively. Blue solid squares and black solid triangles represent the 127 temporary and 128 permanent broadband stations of the NECESSArray, respectively. The temporary stations were deployed under an international collaboration between 09/2009 and 08/2011. The permanent stations are part of the provincial seismic networks operated by the China Earthquake Administration (CEA). The array covers an area of 116°–134° east and 40°–48° north, roughly ~1800 km and ~800 km in the EW and NS direction, respectively. Red volcanic symbols show the three magmatic centers in the area, Wudalianchi, Jingpohu, and Changbaishan, among which Changbaishan is the largest active magmatic center in China. Solid circles indicate major cities in the area. The bottom-right inset shows the motion of the Pacific plate relative to the Eurasia plate. (For interpretation of the references to color in this figure legend, the reader is referred to the web version of this article.)

limited resolution in seismic tomography due to the lack of seismic stations in the area may have partly contributed to this discrepancy. There are only 3 ISC stations in NE China, which were used in the tomography study by Fukao et al. (2003). Several recent studies (Huang and Zhao, 2006; Li and van der Hilst, 2010; Wei et al., 2012) used the provincial networks in the area; station distribution of these networks is, however, highly uneven (black triangles in Fig. 1). There are very few stations inside the Songliao Basin and the great Xing'an Range, which are crucial in resolving the leading edge of the subducting Pacific plate beneath the area. The geometry of the subducting slab in this area is thus not well constrained.

It is known that the Songliao Basin was a rifting basin started at ~157 Ma in late Mesozoic when the shallow subducted Paleo-Pacific plate began to rollback (Ren et al., 2002). Mesozoic volcanic rocks are widely distributed in the region, indicating that active volcanism occurred during the rifting. Volcanism continued in the Cenozoic time in a rather episodic and sporadic manner (Liu et al., 2001). Although it is generally believed that the Cenozoic volcanism in NE China is somehow related to the subduction of the Pacific plate beneath the area, detailed mechanism on the origin of the volcanism, such as the formation of the active Changbai volcano located on the border between China and North Korea, is still not well understood. Based on tomographic imaging using two GSN stations and a small array (18 stations) deployed along the China–North Korea border, Lei and Zhao (2005) found a "columnar low-velocity anomaly extending to 400 km depth" beneath the Changbai volcano and interpreted it as an upwelling from dehydration of the slabs in mantle transition zone, which drives the extension and magmatic activity in the region. Zou et al. (2008) suggested that the piling up and thickening of the stagnant slab in the transition zone could drive asthenospheric upwelling and induce decompression melting at shallow depths. On the other hand, Niu (2005) speculated that edge-driven small-scaled convection along the edges of the Songliao Basin might be responsible for the observed magmatism.

This study is part of the international collaborative project, NECESSArray (the NorthEast China Extended SeiSmic Array), which deployed a total of 127 portable broadband seismographs in NE China. The goal of the project is to build high-resolution seismic images of the mantle beneath NE China in order to better constrain the subduction geometry of the Pacific slab and to understand the formation of the widespread magmatism in the area. In particular, here we intend to delimit cold subducting slabs and hot mantle upwellings within the mantle transition zone by investigating the depth variations of the 410-km and 660-km seismic discontinuities.

The 410-km and 660-km seismic discontinuities that bound the mantle transition zone are thought to be associated with the temperature-sensitive phase transitions from olivine to wadsleyite (e.g., Katsura and Ito, 1989), and from ringwoodite to perovskite plus magnesiowüstite (e.g., Ito and Takahashi, 1989; Katsura et al., 2003), respectively. The latter is also known as the post-spinel transformation. Because these two phase-transitions have a positive and negative Clapeyron slope, respectively, an increase (or decrease) in temperature results in an increase (or de-

crease) in the depth to the 410-km discontinuity and a decrease (or increase) in the depth to the 660-km discontinuity, respectively. Lateral variations in the transition-zone thickness, as well as the depths of the two discontinuities, can provide key information on lateral differences in mantle temperature at 400–700 km depths, and therefore delineate the geometry of a cold slab and a hot upwelling within the mantle transition zone.

Li and Yuan (2003) and Ai et al. (2003) mapped the 660-km discontinuity beneath part of the area using receiver function data recorded by a small array of ∼20 stations deployed along the China–North Korea border. They found that the 660-km is 20 to 30 km deeper near the location of the deepest earthquakes and is relatively shallower to the west, which appears to be contradictory to the tomography images that show a flat slab extending further to the west of the deepest seismicity. The data used by these two studies were, however, not sufficient to determine P- and S-wave velocity in the mantle, so the estimated depth of the 660-km has large uncertainty. The small array also does not provide enough coverage to the west, which is crucial to determine the slab geometry. In this study we used a much larger seismic array to study deep mantle dynamics beneath NE China.

2. Data and analysis

2.1. NECESSArray

We used the waveform data recorded by the NECESSArray, which consists of 127 temporary (blue squares) and 128 permanent broadband stations (black triangles). The 127 temporal PASSCAL/ERI (Earthquake Research Institute, University of Tokyo) stations were deployed under an international collaboration in NE China between September of 2009 and August of 2011. Station information can be found in the supplementary material of Tao et al. (2014). The permanent stations belong to 6 provincial networks of the China Earthquake Administration (CEA) in the study area (Zheng et al., 2009). The array covers an area of 116°–134° east and 40°–48° north, roughly ∼1800 km and ∼800 km in the E–W and N–S direction, respectively (Fig. 1).

We visually examined all the data from earthquakes with M ≥ 5.0, and within the epicentral distance range of 30° to 90° recorded by the PASSCAL/ERI stations between 09/2009 and 08/2011 and by the CEA stations between 07/2007 and 10/2010. We chose a total of 788 earthquakes that were well recorded by the PASSCAL/ERI and CEA stations. These earthquakes provide a good coverage in both distance and azimuth (Fig. 2).

2.2. Receiver functions

We first rotated the two horizontal components of the seismograms to the radial and transverse components. Niu and Li (2011) found a significant portion of the CEA stations had problems in reported orientation of the seismometers. We used their estimates of the sensor orientation at each station, which were determined from P-wave particle motions, to rotate the seismograms recorded from the CEA stations. We further projected the radial and vertical components to the principal directions (longitudinal and in-plane transverse) of the covariance matrix computed from the P-wave data. The receiver functions were then computed from the data projected into this coordinate system (hereafter referred to as P- and SV-component) (Vinnik, 1977; Niu and Kawakatsu, 1998; Niu et al., 2005).

We employed the "water-level" deconvolution technique (Clayton and Wiggins, 1976) to generate receiver functions by a division in frequency domain:

$$RF(\omega) = \frac{V(\omega) \times P^*(\omega)}{\max\{|P(\omega)|^2, \gamma \times |P_{\max}(\omega)|^2\}} e^{-(\frac{\omega}{2\alpha})^2} \quad (1)$$

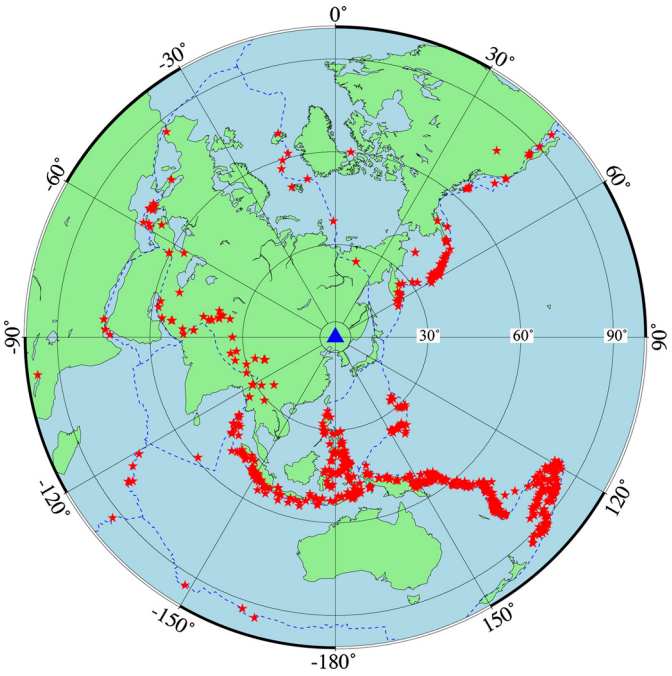

Fig. 2. Distribution of the 788 earthquakes (red stars) used in this study. The blue triangle indicates the center of the seismic array. Note that although the earthquakes seem to be ∼20°–100° away from the array center, we only chose stations in the epicentral distance range of 30° to 90°. (For interpretation of the references to color in this figure legend, the reader is referred to the web version of this article.)

Here γ and α are two constants that define the "water level" and the corner frequency of the Gaussian low pass filter. We set them to 0.01 and 1.5, respectively. $P(\omega)$ and $V(\omega)$ are the spectra of the P and SV components. We used a 100-s time window (5 s before and 95 s after the P wave) to compute the source spectrum of each earthquake. We further screened all the receiver functions with the method of Chen et al. (2010) to eliminate noisy data with low signal-to-noise ratio (SNR) and low coherence. The total number of receiver functions used in the CCP imaging is 45505.

2.3. CCP gathering

Iasp91 Ps moveouts. We applied the CCP stacking technique to receiver function data to map out P-to-S (Ps) conversion events and their lateral variations beneath the array (e.g., Dueker and Sheehan, 1997; Gilbert et al., 2003; Niu et al., 2005; Wang and Niu, 2011). For an assumed conversion depth, d, we first computed the relative arrival time of the converted phase *Pds* with respect to the direct P arrival, as well as the geographic location of the conversion point for each receiver function, by ray tracing the Pds conversion phase using the 1D iasp91 velocity model (Kennett and Engdahl, 1991). We then gathered receiver functions based on the calculated conversion points and computed the Pds conversion coefficient by adding the amplitude of all the receiver functions at the computed Pds relative arrival times.

Parameterization. More specifically, we divided the study area (40°N to 49°N, 115°E to 135°E) into meshed grids of 0.1° by 0.1°, and used a circular cap with a radius of 1 degree for gathering the receiver functions. The total number of the caps is 18 291 (91 × 201), and there are significant overlaps among the caps. This serves as a low-pass filter that smoothens the topographic relief of the two discontinuities with a corner wavelength roughly equivalent to the size of the caps, i.e., ∼200 km. When we summed the receiver functions, instead of adding the single value recorded at the closest

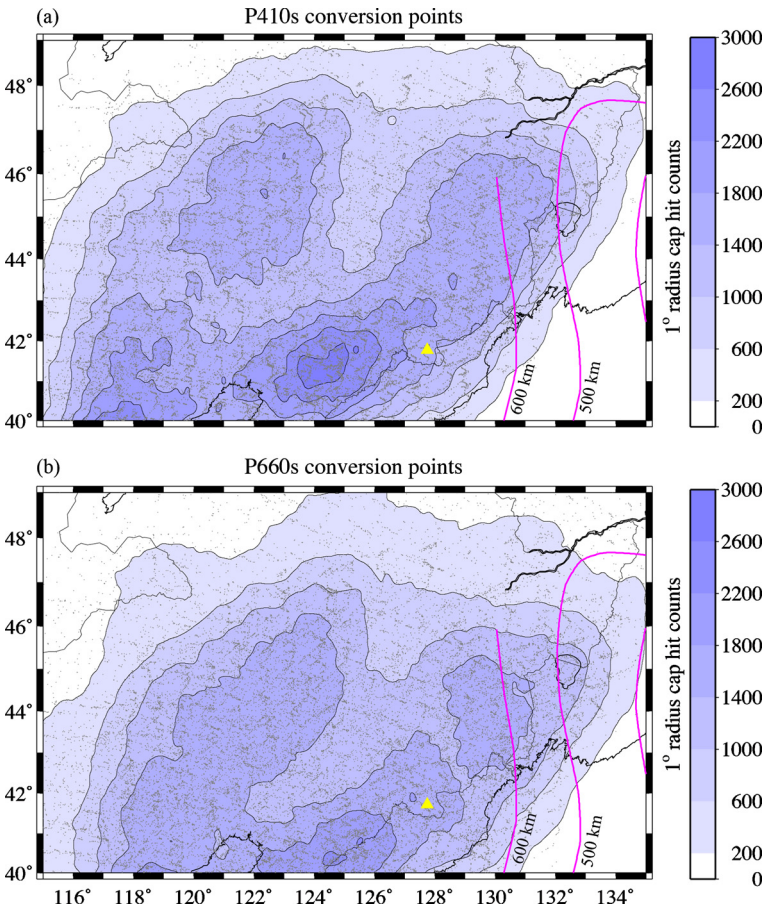

Fig. 3. Map showing hit counts at depths of 410 km and 660 km. Hit counts are defined as the number of receiver functions with P to S conversion points located inside the circular caps. Only the caps with more than 200 hit counts are used in the analysis. Purple lines indicate the Wadati–Benioff zone, showing the geographic location of the subducting Pacific slab at 500 km and 600 km depths. (For interpretation of the references to color in this figure legend, the reader is referred to the web version of this article.)

sampling point to the Pds moveout, we took a 0.2-s long window centered on the arrival time of Pds from each receiver function, stacked them, and took the average value of the stacked receiver function as the Ps conversion coefficient. We varied d from 300 to 800 km in increments of 1 km. Fig. 3 shows the distribution of the Ps conversion points at the 410-km and 660-km discontinuities, together with the hit counts in each cap at the two discontinuities. Most of the study area are sampled by more than 200 receiver functions.

Nth-root stacking. We employed an Nth-root summation technique (Muirhead, 1968) in stacking the 0.2-s long sequences. For the ith grid cap, let $r_k(t)$ represent the kth receiver function gathered in the cap, and t_{dk} is the *Pds* arrival time for a discontinuity with a depth of d, the Nth-root summation, $R_i(d)$, is given by

$$R_i(d) = y_i(d)\left|y_i(d)\right|^{N-1} \tag{2}$$

where

$$y_i(d) = \frac{1}{K}\sum_{k=1}^{K} w_k \operatorname{sign}\left(r_k(t_{dk})\right)\left|r_k(t_{dk})\right|^{1/N} \tag{3}$$

Here K is the total number of receiver functions gathered at the ith cap, and w_k is a Gaussian weight function

$$w_k(d) = \exp\{-x_k^2/a^2\} \Big/ \sum_{n=1}^{K} \exp\{-x_n^2/a^2\} \tag{4}$$

Here x_k is the distance between the cap center (grid) and the conversion point of the kth receiver function. The Gaussian width parameter, a, was set to be the same as the cap radius. We chose $N = 4$ to reduce the uncorrelated noise relative to the usual linear stack ($N = 1$). For example, taking two positive numbers, x and y, the linearly stacking is $(x + y)/2$, which is simply the arithmetic mean. On the other hand, the 2nd-root stack gives the value of $[(x + y)/2 + \sqrt{xy}]/2$, which is the average of the arithmetic and geometric means. Since it takes account of both amplitude and coherence, thus the 2nd-root stacking is expected to be less sensitive to anomalously large noise that may be present in some receiver function data than the linear stack.

3D reference models and their Ps moveouts. Selecting an accurate reference model in computing the moveout corrections are crucial for focusing and locating Ps conversion events. In addition to the 1D iasp91 model (Kennett and Engdahl, 1991), we further employed two 3D tomographic models, one global and one regional, as the reference velocity model in migrating the receiver function data. The global 3D model is the combination of WEPP2' P model from Fukao et al. (2003) and the TXBW S model from Grand (2002). The regional model (hereafter referred to as the NECESS model) is taken from Tang et al. (2014) and was inverted from the traveltime data of the NECESSArray recordings.

We computed the 3D Ps conversion times by superposing the 1D iasp91 traveltimes with a crustal and a mantle correction, which are expected to account for anomalies on the Ps traveltimes due to lateral variations in crustal and mantle structures, respectively.

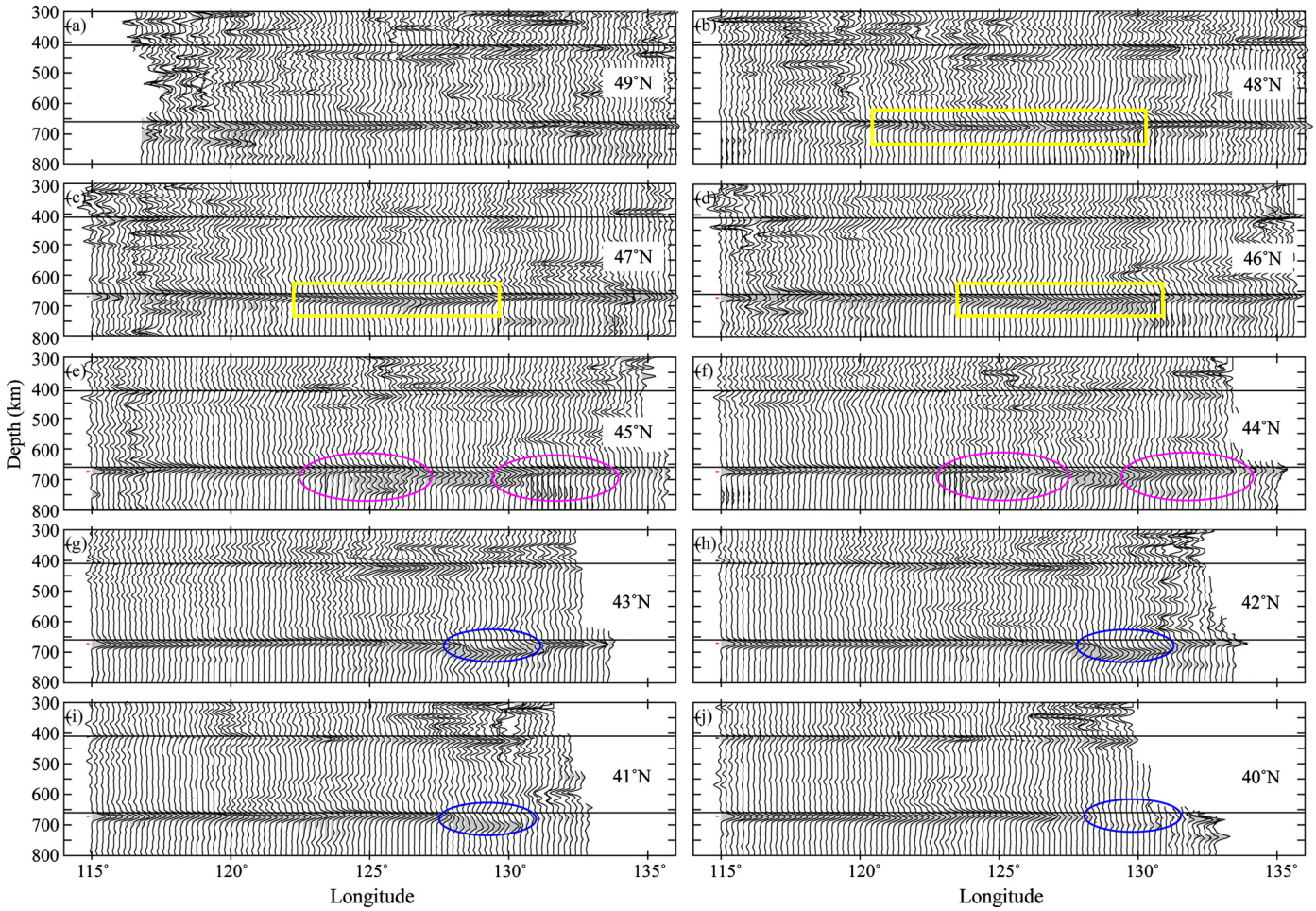

Fig. 4. Depth sections of the CCP gathered receiver functions along latitude from 49°N to 40°N migrated with the 1D iasp91 model. Note the clear P-to-S conversions from the 410-km and 660-km discontinuities, and large variations along the sections. Blue ellipses and yellow boxes indicate the narrow and broad depressions of the 660-km discontinuity observed in the southern and northern parts of the study region. Purple ellipses show the multiple P to S events located at the two sides of the narrow and strong depression in the middle latitudes. (For interpretation of the references to color in this figure legend, the reader is referred to the web version of this article.)

Crustal corrections. We formulated the crustal correction at a station using the Ps conversion time at the Moho, t_{Pms}^{obs}, estimated by Tao et al. (2014), and the deviation of crustal thickness from the iasp91 model:

$$t_c = \left(t_{Pms}^{obs} - t_{Pms}^{iasp91}\right) - \Delta H \cdot K_m$$
$$\text{where } K_m = \frac{\cos\theta_m}{\beta_m} - \frac{\cos\varphi_m}{\alpha_m} \tag{5}$$

where t_{Pms}^{obs} and t_{Pms}^{iasp91}, are the observed and calculated Moho Ps arrival times. ΔH, α_m, and β_m, are the Moho depth anomaly, mantle P- and S-wave velocities, respectively, θ_m and φ_m are the corresponding incident angles of the P and S waves. ΔH can be further approximated by:

$$\Delta H = \left(t_{Pms}^{obs} - t_{Pms}^{iasp91}\right)/K_c$$
$$= \left(t_{Pms}^{obs} - t_{Pms}^{iasp91}\right)\Big/\left(\frac{\cos\theta_c}{\beta_c} - \frac{\cos\varphi_c}{\alpha_c}\right) \tag{6}$$

where α_c and β_c are crustal P- and S-wave velocities, θ_c and φ_c are their corresponding incident angles. Based on Eqs. (5) and (6), the crustal correction can be scaled from the Moho Ps time residual with respect to the iasp91 model:

$$t_c = \left(1 - \frac{K_m}{K_c}\right)\left(t_{Pms}^{obs} - t_{Pms}^{iasp91}\right) \tag{7}$$

We used the iasp91 model to compute K_m and K_c, and for an incoming P wave at teleseismic distance of 60° and a focal depth of 0 km, K_m and K_c roughly equal to 0.103 and 0.122, respectively, resulting in a scaling factor of ~0.156.

Mantle corrections. To compute mantle corrections on the relative *Ps* traveltime, we took the 1D raypaths of the *P* and *Ps* waves computed with the iasp91 model. Based on the block parameterization of the 3D velocity model, we first computed the ray segment in each block and its corresponding segment traveltime. We then calculated the traveltime correction in each block based on the given velocity/slowness perturbation of the 3D model, and finally summed them to obtain the mantle correction of each *P* and *Ps* raypath. In general, the average 1D velocity model of a 3D model differs slightly from the iasp91 model. We confirmed that the relative *Ps* arrival times computed from the average 1D model are close enough to those of the iasp91 model.

With the 3D Ps moveouts, we reconducted the CCP stacking and measured the depths of the two discontinuities from the stacked receiver functions. We compared these values with the iasp91 depths, and referred the differences of the two to as 3D depth corrections. We found that these depth corrections are consistent with the averaged traveltime corrections in each bin when a time-to-depth scaling factor of 10 km per second is used.

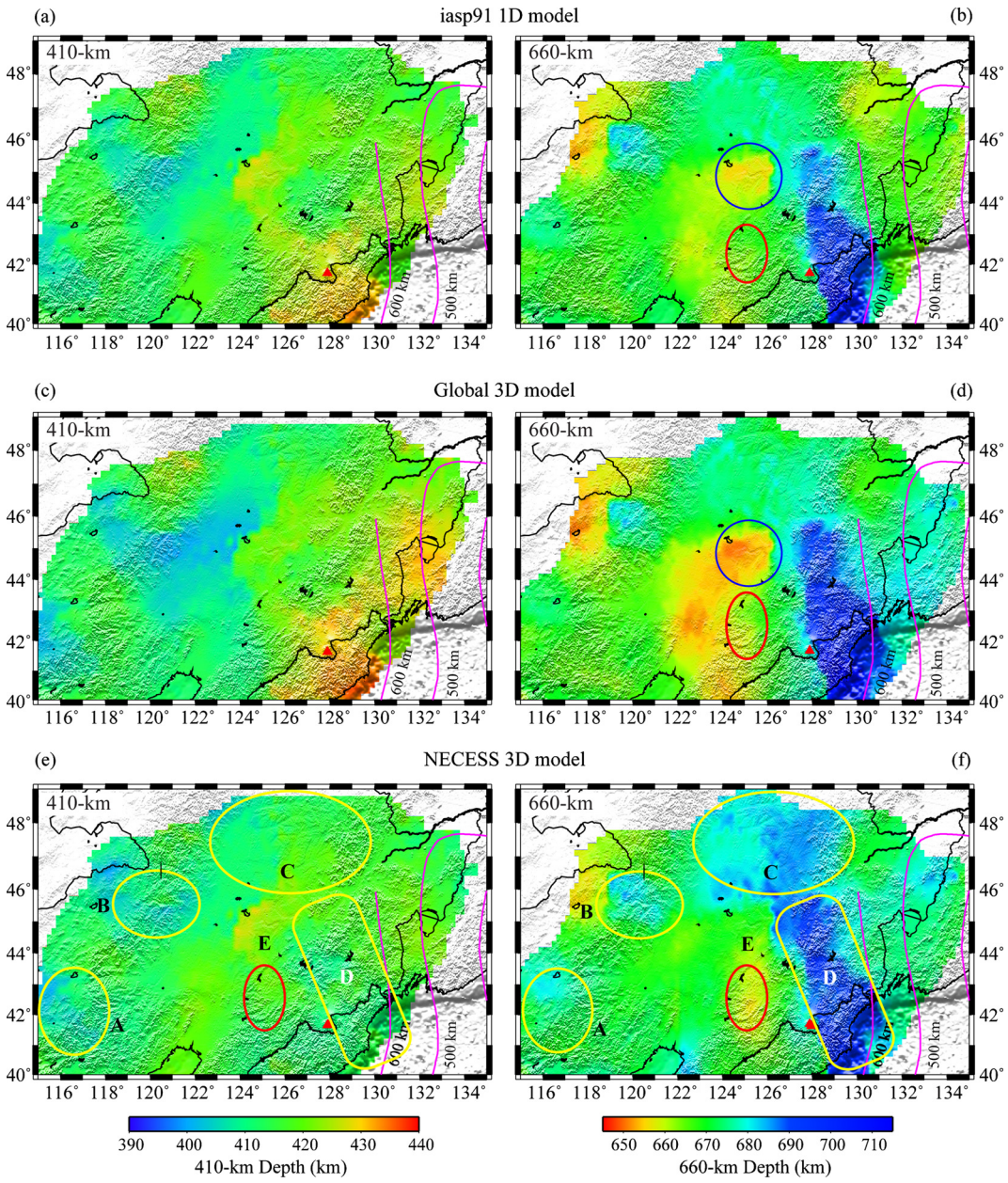

Fig. 5. Maps showing the depth to the 410-km (left, a, c, e), 660-km (right, b, d, f) discontinuities, respectively. The top, middle, and bottom panels show the depths of the two discontinuities migrated from the iasp91, 3D global and NECESS velocity models, respectively. The blue circle shown in (b) and (d) indicates the area where multiple P to S conversion events exist in the CCP images and the depth of the shallowest event is shown here. The yellow ellipses and box marked with A, B, C and D shown in (e) and (f) are anomalous regions with a deeper 660-km discontinuity, while the red ellipse marked E in (e) and (f) is the most prominent region with a shallower 660-km discontinuity. (For interpretation of the references to color in this figure legend, the reader is referred to the web version of this article.)

3. Results

3.1. CCP migration with iasp91

In general, the P-to-S conversions at the 410-km and 660-km discontinuities can be seen clearly on most of the CCP stacks, as shown in Fig. 4. In all the depth cross sections the 660-km discontinuity is well imaged while the 410-km is clearly seen at low latitudes, and becomes quite complicated as moving towards north. This is especially true in the northernmost latitudes (48° and 49°) and the corners, where P410s becomes difficult to be picked. In the southern part of the study area, as shown in the lower part of Fig. 4, the 660-km displays a substantial and localized depression of ~30–50 km in the longitudinal range of ~128° to 131° (blue ellipses in Figs. 4g–4j). To the west of the depression, at longitude of ~125°, the 660-km discontinuity is slightly uplifted as compared to further west. On the other hand, the depression becomes less substantial and broader as it gradually approaches to the north (yellow rectangles in Figs. 4b–4d). In the middle latitudes, we also found other strong P-to-S conversions below the 660-km at the two sides of the depression (pink ellipses in Figs. 4e and 4f).

We manually picked the depths of the two discontinuities from bins with a hit count of ≥200. The lateral variations of the two discontinuities are shown in Figs. 5a and 5b, respectively. Interpolation is applied for a small number of grids (less than 0.8% of the total grids) whose stacks do not show robust P410s or P660s. The depth of the 410-km discontinuity varies between 403 km and 434 km with an average value of 417 km, while the 660-km is located between 651 km and 706 km deep below the surface and has an average depth of 670 km. The most prominent depth anomaly of the 660-km is located in the western end of the

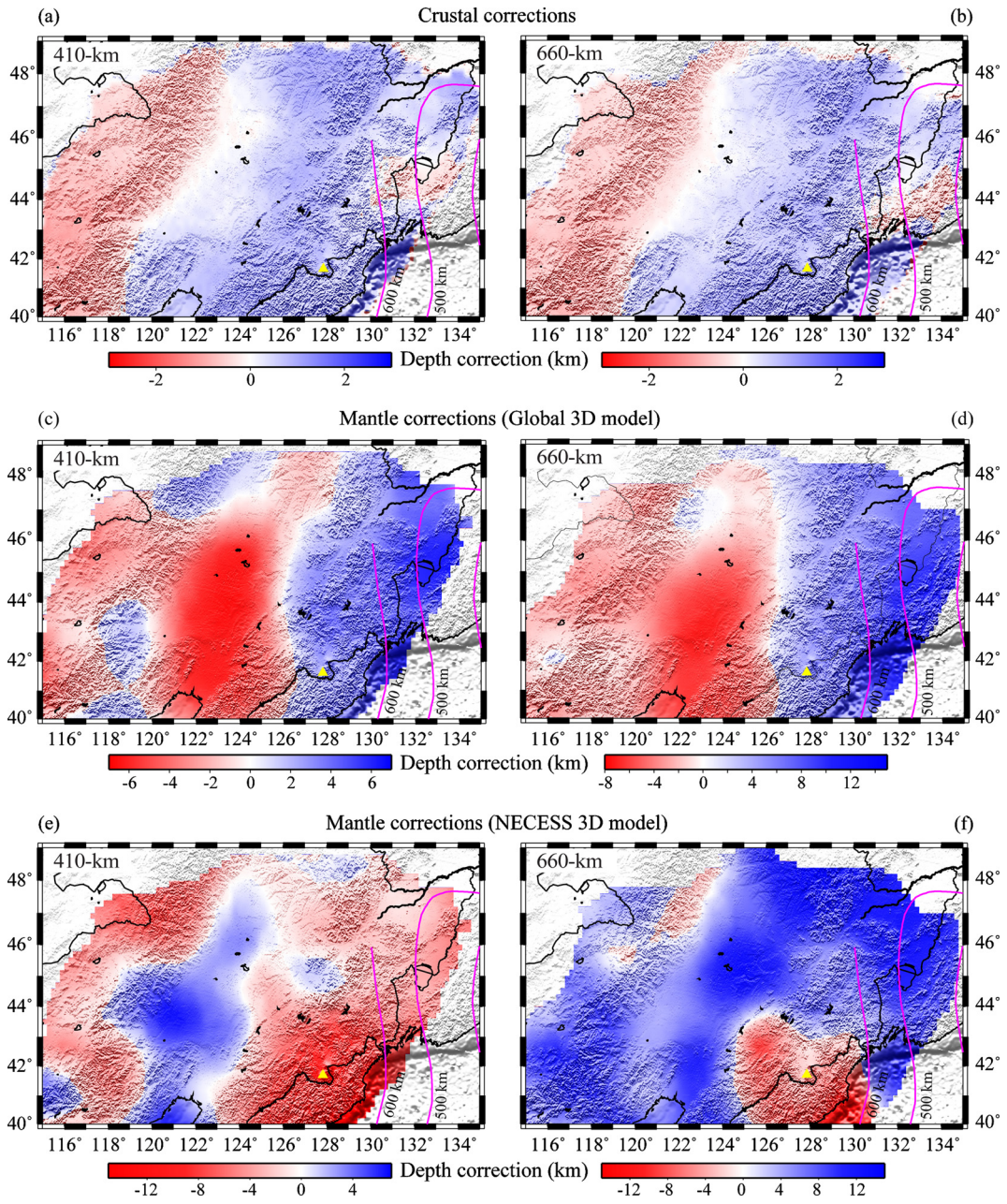

Fig. 6. Depth corrections on the 1D migration depth of the 410-km (left) and 660-km (right) computed from the observed Moho Ps arrival times (a–b); the global 3D model (c–d); and the NECESS 3D model (e–f). Red and blue indicate negative and positive corrections to the depths derived from the 1D iasp91 model, respectively. (For interpretation of the references to color in this figure legend, the reader is referred to the web version of this article.)

deep seismicity, where the upper- and lower-mantle boundary is ~30–50 km deeper than the global average, ~660 km (Flanagan and Shearer, 1998). The depression is elongated along the strike of the Pacific slab and is confined within a ~250 km wide area in the E–W subduction direction. Approximately 200–300 km west of the depression, the 660-km is slightly uplifted by a few kilometers. The most visible uplift is seen at around 45°N where multiple peaks are present in the stacked receiver functions as mentioned above, and the depth shown here is picked from the most prominent conversion, which is the shallower one.

3.2. Crustal corrections

Tao et al. (2014) found that the *Pms* residual time varies from −1.17 to 1.41 s, which converts to a crustal correction of −0.18 to 0.22 s if we use a scaling factor of ~0.156. We restacked the receiver functions gathered in each bin using the corrected *P410s* and *P660s* moveouts. The migrated depth of the two discontinuities differs from the iasp91 estimates only by a few kilometers (within ±2.5 km). Figs. 6a and 6b show the depth corrections to the 410-km and 660-km discontinuities due to the crustal structure in the study area. Since the geographic location of the Ps conversion point changes with depth and the receiver functions used to stack P410s and P660s at each grid are different from each other, we anticipated different crustal corrections for the two discontinuities. However, the difference appears to be rather trivial, as shown in Figs. 6a and 6b. Tao et al. (2014) found that the crust beneath the Great Xing'an Range is much thicker (~40 km) than that below the Songliao Basin and the eastern part of the study area. This pattern is well seen in Figs. 6a and 6b. Negative corrections are located at the Great Xing'an Range in the west side of

the Songliao Basin, whereas the Songliao Basin and the east part of the study area are featured by a positive correction of ∼2 km.

3.3. CCP migration with the global 3D model

Figs. 6c and 6d show the lateral variations of the depth correction computed from the global 3D model, which range from ∼−7 to ∼7 km for the 410-km, and from ∼−7 to ∼16 km for the 660-km, respectively. In both depths, the positive corrections are distributed in the east where high velocity anomalies associated with the subducting Pacific plate are imaged by the global model, and the corrections in the west part of the study area including the Songliao Basin are predominantly negative.

The depth variations of the corrected 410-km and 660-km are shown in Figs. 5c and 5d, respectively. Because of the corrections, the narrow depression on the 660-km in the front of the deep seismicity (Fig. 5d) becomes more prominent than that of the iasp91 image (Fig. 5b). The depression roughly follows the 600-km-deep contour line of the Wadati–Benioff zone in the N–S direction, and terminates at the northern end of the deep seismicity. Since the mantle corrections inside the Songliao Basin and its southeastern edge are negative, the uplift on the 660-km beneath the basin (Fig. 5d) becomes more prominent than that observed on the iasp91 image (Fig. 5b). We found that most of the mantle corrections seem to come from the S-wave model, which has relatively poor resolution in the study area due to lack of data coverage, thus it is very likely that the uncertainties in the corrections are as large as their amplitudes. In fact, we did not find any significant increase in the amplitude of the stacked P410s and P660s phases with the global 3D moveouts.

3.4. CCP images with the NECESS model

The NECESS model was derived from the absolute and relative travel times of P and relative travel times of the S waves recorded by the array (Tang et al., 2014). The P-wave data were inverted together with the global ISC traveltime data, while the S data included only the NECESSArray data, and the two were inverted independently. Based on resolution tests and 3D waveform modeling, Tang et al. (2014) found that the observed waveform variations of the SH wave across the array are better explained by a modification of the S model (TZ2S) with doubled velocity perturbations below the 400 km depth. As such, we used the TZ2S model as the reference S-wave model. The corrections on the depth of the two discontinuities are ∼−15–6 km for the 410-km (Fig. 6e) and ∼−13–15 km for the 660-km (Fig. 6f), respectively. The largest depth correction on the 410-km is observed beneath the Changbaishan volcanic complex, which is underlain by a substantial low velocity column extending from the surface to the transition zone, according to Tang et al. (2014). The corrections to the depth of the 660-km discontinuity are predominantly positive except for the Changbaishan area.

Figs. 5e and 5f show the topographic maps of the two discontinuities with the NECESS 3D model. The 660-km discontinuity shows a similar narrow and prominent depression in the south as mentioned before. In the northern part, there is a broad but moderate depression (∼20 km) in the longitudinal range of ∼123° to ∼129°E. On the other hand, the map shows an eminent topographic high centered around 43°N, 125°E (the red ellipse in Fig. 5f) due to a negative depth correction, whereas the other uplifts, especially the one at around 45°N, 125°E (the blue circle shown in Figs. 5b and 5d) are absent here.

4. Discussion

In addition to the two upper mantle discontinuities, there are several intermittent negative pulses at depth between 300 and 400 km (Fig. 4), which may represent true structures in the upper mantle. A low-velocity layer above the 410-km discontinuity has been observed beneath many locations (e.g., Revenaugh and Sipkin, 1994; Song et al., 2004; Jasbinsek and Dueker, 2007; Tauzin et al., 2010). However, many stations used in the stacking here are located inside the Songliao Basin. The underlying sediment beneath these stations can generate strong reverberations on receiver function that may extend to ∼30–35 s after the P wave. The potential interference between the reverberations and the deep Ps conversions makes it difficult to determine the nature of the observed negative pulses.

Between 42°N to 45°N latitudes, we also found other strong P-to-S conversions below the 660-km at the two sides of the depression (pink ellipses in Figs. 4e and 4f). Observation of multiple velocity jumps at depths between 650 km and 750 km have been reported by many studies. Niu and Kawakatsu (1996) found a complicated 660-km at the tip of the subducting Pacific plate beneath NE China, and suggested that the observed velocity jumps are likely caused by multiple phase transitions of olivine and garnet. The geographic locations of the multiple jumps are consistent with the one reported by Niu and Kawakatsu (1996). However, since the multiple conversions are observed around the two sides of the depression, and the CCP gathering assumes flat layers in locating P-to-S conversion sources, it is difficult to determine whether or not the multiple conversions are caused by diffractions at the corners of the depression. We also note that such multiples are not seen in the southern latitude, where the depression is also prominent. Thus we felt that these multiples, together with the negative pulses above the 410-km, require further investigations in order to understand their nature, which is beyond the scope of this study. Here we focus our discussion on the 410-km and 660-km discontinuities and their relationships with the Pacific subduction and mantle upwelling.

It is known that the estimates of the absolute depths of the two discontinuities depend highly on the assumed P- and S-wave velocity (especially their ratio) in converting Ps traveltimes to depths. Since the uppermost 400 km of the mantle is well known for the presence of strong lateral heterogeneities, the estimated depths of the 410-km and 660-km discontinuities could have large uncertainties due to unmodeled velocity structures above the 410-km discontinuity. Estimates on the transition zone thickness, on the other hand, are generally thought to be more or less correct, as lateral heterogeneities inside the transition zone are relatively smaller than those of the upper mantle. We found that the corrections on transition zone thickness computed from the 3D global model range from −4 to 10 km (Fig. 7). Most of the large corrections are located at the southeastern edge of the study area due to slab-related high-velocity anomalies within the transition zone. Also in the corners, the incoming rays are limited to certain directions, such that the time-to-depth migration can be easily affected by anomalous structures along the raypath (Fig. 7a). Overall, the corrections are within ±5 km, therefore the thickness maps of the transition zone derived from the 1D iasp91 model (Fig. 7c) and 3D global model (Fig. 7d) are nearly identical.

On the other hand, the corrections computed from the NECESS model vary from −5 to 17 km (Fig. 7b). The corrections are predominantly positive across the study area except for two spots. One of the spots is located at around 43°N, 125°E (red ellipse in Fig. 7b), and is caused primarily by a continuous low-velocity column extending across the transition zone (Fig. 7f) (Tang et al., 2014). The S-wave velocity perturbations inside the column are much larger than those of P wave, resulting in a large anomaly in the Ps traveltime. Waveform modeling of the NECESSArray recordings of two earthquakes from southwest Pacific indicated that the S-wave velocity contrast between the low velocity column and its surrounding areas can reach as much as 8% (Tang et al., 2014).

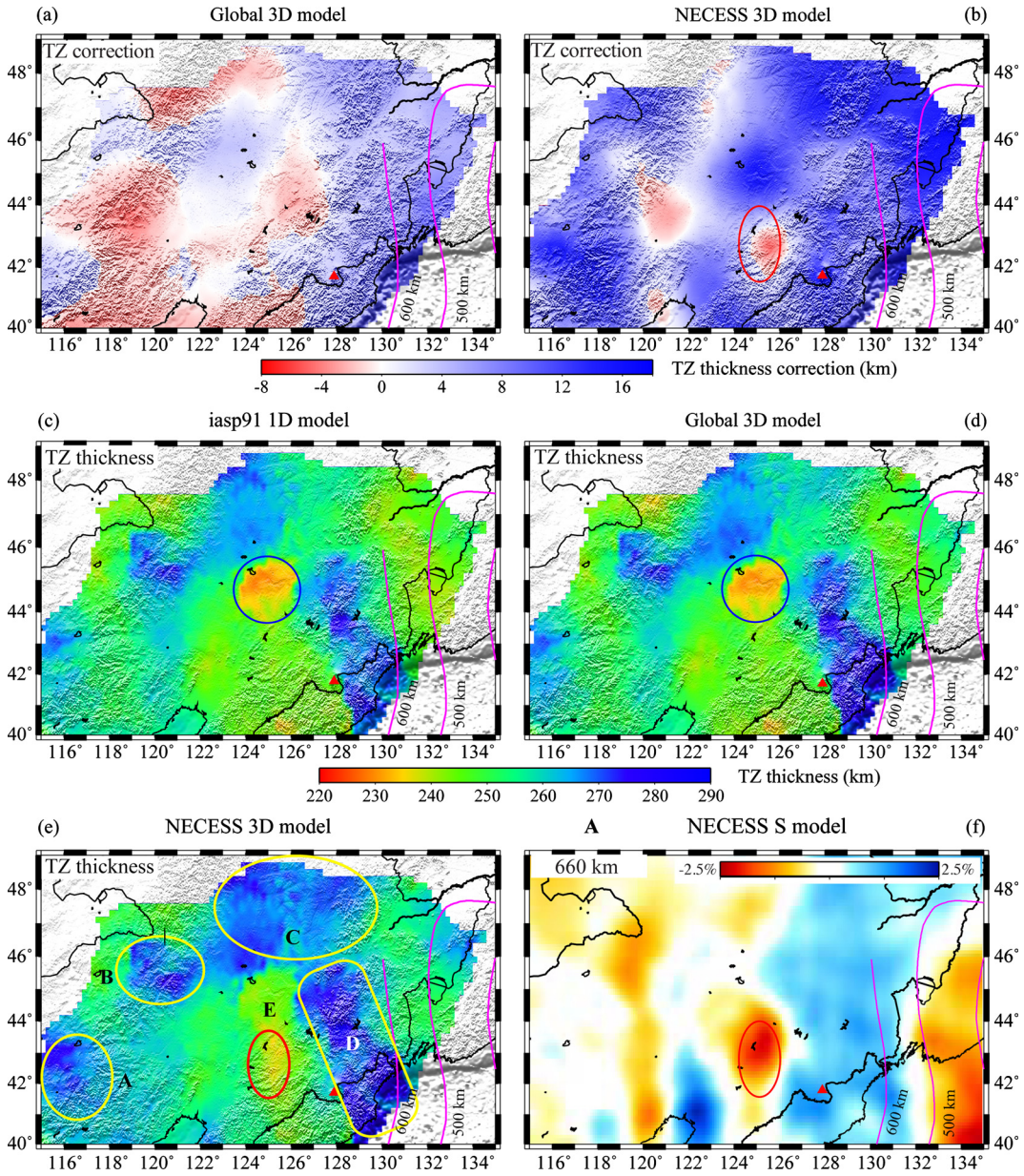

Fig. 7. Corrections on transition zone thickness computed from the 3D global P and S-wave models (a) and the NECESSArray 3D P and S wave models (b). Red and blue represent negative and positive corrections, respectively. Note the large difference between (a) and (b). Transition zone thickness migrated with the 1D iasp91 model (c), the global 3D model (d) and NECESS 3D models (e). Red and blue indicate thin and thick transition zone, respectively. Transition zone thickness computed with the 1D iasp91 model and the global 3D model roughly shows similar distribution due to the small correction shown in (a). Multiple Ps conversion events are observed in the area marked with the blue circle in (c) and (d), and the depths of the shallowest event are used in computing the transition zone thickness here, resulting in a relatively thin transition zone in this part of the study area. (f) S-wave velocity perturbations at 660 km depth from the NECESS S model (Tang et al., 2014). Red and blue indicate slow and fast velocity anomalies, respectively. (For interpretation of the references to color in this figure legend, the reader is referred to the web version of this article.)

Thus it might not be always suitable to use a 1D model to estimate transition zone thickness in regions such as subduction zones where the transition zone could be strongly heterogeneous. The lateral distribution in transition zone thickness migrated with the 3D NECESS model is shown in Fig. 7e, which correlates well with the depth of the 660-km discontinuity shown in Fig. 5f.

We checked the amplitude of the CCP stacks migrated with the iasp91, the global and NECESS models and found that the NECESS P660s generally has the highest average amplitude among the three migrations (average amplitude ratio $A_{P660s\_NECESS}/A_{P660s\_iasp91} = 1.10$, $A_{P660s\_global}/A_{P660s\_iasp91} = 0.97$). Thus it is reasonable to assume that the depths migrated from the NECESS model better reflect the true depths of the two discontinuities.

The depth of the 410-km discontinuity migrated from the NECESS model varies from 400 to 428 km with an average of 414 km (Fig. 5e), while the 660 km is located in the depth range between 654 km and 700 km, with an average depth of 674 km (Fig. 5f). The transition zone thickness varies from 239 to 288 km, with an average of 261 km (Fig. 7e). In the southwestern (A in Figs. 5e and 5f) and northwestern (B in Figs. 5e and 5f) edges, the 410-km appears to be uplifted by a few kilometers while the 660-km is depressed by the similar amount, resulting in a thick transition zone beneath the two areas (A and B in Fig. 7e). However, as shown in Fig. 4, the stacked amplitude of P410s in the region B is generally low, depth of the 410-km discontinuity thus might not be well constrained in this area. The anti-correlation between the depths of the two discontinuities indicates a cold tran-

sition zone beneath southwestern part of the Great Xing'an Range. Tang et al. (2014) found a westward dipping fast-velocity anomaly beneath the same area. The anomaly runs across the 410-km and extends nearly to the 660-km discontinuity with a high dipping angle, which is consistent with what we observed here.

The most prominent anomaly in the estimated depth of the 660-km discontinuity as well as in the transition zone thickness lies at the extension of the deepest seismicity of the Wadati–Benioff zone (region D in Figs. 5f and 7e). The 660-km discontinuity is depressed by ~40 km compared to the global average. If we use a Clapeyron slope of −2.0 MPa/K (Litasov et al., 2006) for the ringwoodite-to-perovskite phase change, then the observed 40 km depression corresponds to a 667 K temperature anomaly as compared to the global average. Kawakatsu and Yoshioka (2011) calculated the temperature profile of the subducting slab beneath the Japan Trench and showed that the temperature difference between the slab and surrounding mantle in the transition zone is around 650 K, which is roughly consistent with the estimate here. The region with narrow and strong depression ends at around 45.5°N, where the 600 km contour line of the Wadati–Benioff zone terminates. We also noticed that the elongated region of depression has a slightly different orientation from the N–S strike of the deep Wadati–Benioff zone (Fig. 5f).

In the northern area (region C in Figs. 5f and 7e), we found that the 660-km is moderately depressed by ~20 km in a broader area along the E–W direction, as compared to the south. This difference in the depression of the 660-km discontinuity is consistent with the lateral distribution of high-velocity anomalies at the base of the transition zone in the 3D NECESS model. Both tomography and receiver function images thus suggest that slab stagnation might not be a pervasive feature of deep subduction in the study area. In the southern part where the Wadati–Benioff zone seismicity can be traced down to 600 km deep, we found that slab stagnation inside the transition zone is rather limited, within 200–300 km in the E–W direction, due to either slab sinking into the lower mantle or a lateral tear-off of the slab. To the north, the slab seems to extend further west such that the subducted Pacific plate is stagnant in this part of the area. It is, however, difficult to determine whether the stagnant slab in this area is associated with the current stage or a previous episode of subduction.

Another prominent anomaly of the 660-km discontinuity is the 5–10 km uplift located at about 200 km west to the depression. It is an N–S elongated feature that centers at 43°N and 125°E with a lateral extension of ~100 km by ~200 km along the E–W and N–S directions, respectively. The uplift almost collocates with the strong S-wave velocity anomaly at the same depth. Tang et al. (2014) argued that the uplift of the 660-km and lower velocity were caused by a mid-mantle upwelling, which is a flow of hot sub-lithospheric mantle that has been carried down to the transition zone underneath the subducting slab. When a gap in the subducting slab is present, the buoyant sub-lithospheric mantle escapes from the slab sealing and rises up to form a mantle upwelling.

5. Conclusions

We investigated the mantle transition zone structure beneath the NE China with receiver function data recorded by the broadband NECESSArray. The 660-km discontinuity imaged by the receiver functions shows two important features: (1) a narrow and strong depression along the extension of the deep seismicity between ~40°N and ~45.5°N, and a broad but moderate depression in the north; (2) a moderate and localized uplift centered at ~43°N and 125°E, about ~200 km west to the Changbaishan volcanic complex. Areas with a depressed and an uplifted 660-km match well with high- and low-velocity regions, respectively, in the tomography maps. Our results suggest that slab geometry changes significantly along the strike of the subduction and there is a lack of a flat-lying slab at the base of the transition zone in the southern part of the study area where the Changbaishan volcanic complex is located. Our observations also suggest that the Changbaishan volcanism is unlikely originated from dehydration of the flat-lying Pacific slab, but agree with a scenario where magmatism is fed by a mantle upwelling from just below the 660-km discontinuity.

Acknowledgements

We thank all the people in the NECESSArray project for installing and servicing the seismic array. The waveform data of the permanent stations were provided by the China Seismic Array Data Management Center at the Institute of Geophysics, China Earthquake Administration. We also thank two anonymous reviewers for their constructive comments and suggestions, which significantly improved the quality of this paper. L.Z., J.N. Y.C. were supported by NSFc grants 40821062 and 90814002. F.N. was supported by NSF EAR-0635666 and the China University of Petroleum at Beijing (NSFC41274099). S.G. and J.N. were supported by NSF EAR-0635855 and EAR-0634903, respectively, H.K., S.T., and M.O. were supported by the JSPS grant 19104011.

References

Ai, Y., Zheng, T., Xu, W., He, Y., Dong, D., 2003. A complex 660 km discontinuity beneath northeast China. Earth Planet. Sci. Lett. 212, 63–71.

Chen, Y., Niu, F., Liu, R., Huang, Z., Tkalcic, H., Sun, L., Chan, W., 2010. Crustal structure beneath China from receiver function analysis. J. Geophys. Res. 115, B03307. http://dx.doi.org/10.1029/2009JB006386.

Clayton, R.W., Wiggins, R.A., 1976. Source shape estimation and deconvolution of teleseismic body waves. Geophys. J. R. Astron. Soc. 47, 151–177.

Dueker, K.G., Sheehan, A.F., 1997. Mantle discontinuity structure from midpoint stacks of converted P and S waves across the Yellowstone hotspot track. J. Geophys. Res. 102, 8313–8328.

Engebretson, D.C., Kelley, K.P., Cashman, H.J., Richards, M.R., 1992. 180 million years of subduction. GSA Today 2, 93–95.

Flanagan, M., Shearer, P., 1998. Global mapping of topography on transition zone velocity discontinuities by stacking SS precursors. J. Geophys. Res. 103, 2673–2692.

Fukao, Y., To, A., Obayashi, M., 2003. Whole mantle P wave tomography using P and PP-P data. J. Geophys. Res. 108 (B1), 2021. http://dx.doi.org/10.1029/2001JB000989.

Gilbert, H.J., Sheehan, A.F., Dueker, K.G., Molnar, P., 2003. Receiver functions in the western United States, with implications for upper mantle structure and dynamics. J. Geophys. Res. 108, 2229. http://dx.doi.org/10.1029/2001JB001194.

Grand, S.P., 2002. Mantle shear-wave tomography and the fate of subducted slabs. Philos. Trans. R. Soc. Lond. A 360, 2475–2491.

Huang, J., Zhao, D., 2006. High-resolution mantle tomography of China and surrounding regions. J. Geophys. Res. 111, B09305. http://dx.doi.org/10.1029/2005JB004066.

Ito, E., Takahashi, E., 1989. Postspinel transformations in the system Mg_2SiO_4–Fe_2SiO_4 and some geophysical implications. J. Geophys. Res. 94, 10637–10646.

Jasbinsek, J., Dueker, K., 2007. Ubiquitous low-velocity layer atop the 410-km discontinuity in the northern Rocky Mountains. Geochem. Geophys. Geosyst. 8, Q10004. http://dx.doi.org/10.1029/2007GC001661.

Katsura, T., Ito, E., 1989. The system Mg_2SiO_4–Fe_2SiO_4 at high pressures and temperatures: precise determination of stabilities of olivine, modified spinel, and spinel. J. Geophys. Res. 94, 15663–15670.

Katsura, T., Yamada, H., Shinmei, T., Kubo, A., Ono, S., Kanzaki, M., Yoneda, Y., Walter, M.J., Ito, E., Urakawa, S., Funakoshi, K., Utsumi, W., 2003. Post-spinel transition in Mg_2SiO_4 determined by high P-T in situ X-ray diffraction. Phys. Earth Planet. Inter. 136, 11–24.

Kawakatsu, H., Yoshioka, S., 2011. Metastable olivine wedge and deep dry cold slab beneath southwest Japan. Earth Planet. Sci. Lett. 303, 1–10.

Kennett, B.L., Engdahl, E.R., 1991. Travel times for global earthquake location and phase identification. Geophys. J. Int. 105, 429–465.

Lei, J., Zhao, D., 2005. P-wave tomography and origin of the Changbai intraplate volcano in Northeast Asia. Tectonophysics 397, 281–295.

Li, C., van der Hilst, R.D., 2010. Structure of the upper mantle and transition zone beneath Southeast Asia from traveltime tomography. J. Geophys. Res. 115, B07308. http://dx.doi.org/10.1029/2009JB006882.

Li, X., Yuan, X., 2003. Receiver functions in northeast China – implications for slab penetration into the lower mantle in northwest Pacific subduction zone. Earth Planet. Sci. Lett. 216, 679–691.

Litasov, K.D., Ohtani, E., Sano, A., 2006. Influence of water on major phase transitions in the Earth's Mantle. In: Jacobsen, S.D., van der Lee, S. (Eds.), Earth's Deep Water Cycle, vol. 168. AGU, Washington, DC, pp. 95–111.

Liu, J., Han, J., Fyfe, W.S., 2001. Cenozoic episodic volcanism and continental rifting in northeast China and possible link to the Japan Sea development as revealed from K–Ar geochronology. Tectonophysics 339, 385–401.

Muirhead, K., 1968. Eliminating false alarms when detecting seismic events automatically. Nature 217, 533–534.

Niu, Y., 2005. Generation and evolution of basaltic magmas: some basic concepts and a new view on the origin of Mesozoic–Cenozoic basaltic volcanism in Eastern China. Geol. J. China Univ. Geosci. 11, 9–46.

Niu, F., Kawakatsu, H., 1996. Complex structure of mantle discontinuities at the tip of the subducting slab beneath Northeast China: a preliminary investigation of broadband receiver functions. J. Phys. Earth 44, 701–711.

Niu, F., Kawakatsu, H., 1998. Determination of the absolute depths of the mantle transition zone discontinuities beneath China: effect of stagnant slabs on mantle transition zone discontinuities. Earth Planets Space 50, 965–975.

Niu, F., Li, J., 2011. Component azimuths of the CEArray stations estimated from P wave particle motion. Earthq. Sci. 24, 3–13. http://dx.doi.org/10.1007/s11589-011-0764-8.

Niu, F., Levander, A., Ham, S., Obayashi, M., 2005. Mapping the subducting Pacific slab beneath southwest Japan with Hi-net receiver functions. Earth Planet. Sci. Lett. 239, 9–17.

Ren, J., Tamaki, K., Li, S., Zhang, J., 2002. Late Mesozoic and Cenozoic rifting and its dynamic setting in Eastern China and adjacent areas. Tectonophysics 344, 175–205.

Revenaugh, J., Sipkin, S.A., 1994. Seismic evidence for silicate melt atop the 410-km mantle discontinuity. Nature 369, 474–476. http://dx.doi.org/10.1038/369474a0.

Song, T.A., Helmberger, D.V., Grand, S.P., 2004. Low velocity zone atop the 410 seismic discontinuity in the northwestern United States. Nature 427, 530–533.

Tang, Y., Obayashi, M., Niu, F., Grand, S.P., Chen, Y.J., Kawakatsu, H., Tanaka, S., Ning, J., Ni, J.F., 2014. Seismic evidence of a subduction-induced mid-mantle plume for the origin of Changbaishan volcanism in northeast China. Nat. Geosci. 7, 470–475. http://dx.doi.org/10.1038/ngeo2166.

Tao, K., Niu, F., Ning, J., Chen, Y.J., Grand, S.P., Kawakatsu, H., Tanaka, S., Obayashi, M., Ni, J.F., 2014. Crustal structure beneath NE China imaged by NECESSArray receiver function data. Earth Planet. Sci. Lett. 398, 48–57. http://dx.doi.org/10.1016/j.epsl.2014.04.043.

Tauzin, B., Debayle, E., Wittlinger, G., 2010. Seismic evidence for a global low-velocity layer within the Earth's upper mantle. Nat. Geosci. 3, 718–721. http://dx.doi.org/10.1038/ngeo969.

Vinnik, L.P., 1977. Detection of waves converted from P to SV in the mantle. Phys. Earth Planet. Inter. 15, 39–45.

Wang, X., Niu, F., 2011. Imaging the mantle transition zone beneath eastern and central China with CEArray receiver functions. Earthq. Sci. 24, 65–75.

Wei, W., Xu, J., Zhao, D., Shi, Y., 2012. East Asia mantle tomography: new insights into plate subduction and intraplate volcanism. J. Asian Earth Sci. 60, 88–103. 2012.

Zheng, X., Ouyang, B., Zhang, D., Yao, Z., Liang, J., Zheng, J., 2009. Technical system construction of Data Backup Centre for China Seismograph Network and the data support to researches on the Wenchuan earthquake. Chin. J. Geophys. 52, 1412–1417. http://dx.doi.org/10.3969/j.issn.0001-5733.2009.05.031 (in Chinese).

Zou, H., Fan, Q., Yao, Y., 2008. U–Th systematics of dispersed young volcanoes in NE China: asthenosphere upwelling caused by piling up and upward thickening of stagnant Pacific slab. Chem. Geol. 255, 134–142.